SUPPLEMENTARY MATERIAL

Modelling approach

The two-dimensional numerical experiments are carried out with the *I2ELVIS* code, which solves the continuity, momentum and heat conservation equations using the finite-difference/marker-in-cell method (Gerya & Yuen, 2003; 2007). A description of all symbols from the following equations are listed in **Supplementary Table 1**, while details on parameters used in the models are presented in **Supplementary Table 2**.

The continuity and momentum (i.e., Stokes formulation) equations are solved on a staggered Eulerian grid and have the form:

$$\frac{D\,ln\,\rho_{eff}}{Dt} + \frac{\partial v_i}{\partial x_i} = 0\ , \qquad (1)$$

$$-\frac{\partial P}{\partial x_i} + \frac{\partial \sigma_{ij}}{\partial x_i} = -\rho_{eff}\, g_i\ . \qquad (2)$$

The heat conservation equation is expressed in a Lagrangian form to avoid numerical diffusion of temperature:

$$\rho_{eff}\, C_P\, \frac{\mathrm{D}T}{\mathrm{D}t} = -\frac{\partial q_i}{\partial x_i} + H_r + H_a + H_s\ , \qquad (3)$$

with q_i the heat flux solved as:

$$q_i = -k\,\frac{\partial T}{\partial x_i}\ . \qquad (4)$$

All the lithologies in the experiments deform according to a visco-elasto-plastic rheological formulation, implying that the deviatoric strain rate tensor $\dot{\varepsilon}_{ij}$ includes the three respective components:

$$\dot{\varepsilon}_{ij} = \dot{\varepsilon}_{ij_{viscous}} + \dot{\varepsilon}_{ij_{elastic}} + \dot{\varepsilon}_{ij_{plastic}}\ . \qquad (5)$$

Details on the calculation of the rheological constitutive equations are available in Gerya & Yuen (2007). However, it is worth noting that implemented fluid propagation (see details below) affects the rock rheology by lowering the plastic strength σ_{yield}, which limits the creep viscosity such that:

$$\eta_{eff} \leq \frac{\sigma_{yield}}{2\,\dot{\varepsilon}_{II}} , \tag{6}$$

with

$$\eta_{eff} = \dot{\varepsilon}_{II}^{\frac{1-n}{n}} A_D^{\frac{1}{n}} exp\left(\frac{E+P\,V}{n\,R\,T}\right) , \tag{7}$$

and

$$\sigma_{yield} = C + P\,sin\left(\varphi_{dry}\right)(1 - \lambda_{fluid}) . \tag{8}$$

Altogether, these equations allow to approximate the permanent, brittle and ductile deformation, which is strongly affected by the presence of fluid markers within the computational domain.

One key aspect in these experiments is therefore the implementation of hydration/dehydration processes, fluid transport and fluid weakening effects which are of paramount importance in subduction-related tectonic processes (Peacock, 1990; Saffer & Tobin, 2011). Fluids are initially prescribed in the subducting oceanic lithosphere as (i) pore water in sediments and basaltic crust ($X_{w_{pore}}$ = 1 wt. %) and (ii) mineral bound water in sediments, basaltic crust and gabbroic crust. Pore-water release is assumed constant from 0 to 75 km depth, mimicking compaction and dehydration from low-temperature metamorphic reactions (e.g., smectite-illite and opal-quartz transformations; Moore & Vrolijk, 1992). Bound water release is calculated by free-energy minimization as a function of pressure, temperature and rock type (Connolly, 2005; Gerya & Meilick, 2011). Resulting free water is then transported as newly-formed Lagrangian markers, according to the viscous velocity (i.e., describing the momentum of the surrounding rock markers), the fluid buoyancy and the dynamic pressure gradients, such that:

$$v_{i_{water}} = v_i + v_{perc}\,k_i , \tag{9}$$

with k_i coefficient calculated as:

$$k_i = \frac{\rho_{crust}\, g_i - \frac{\partial P}{\partial x_i}}{(\rho_{crust} - \rho_{fluid})\, g_y} \, . \tag{10}$$

Once moving, fluid markers may be then consumed by rock markers (either as pore or mineral bound water), depending on their stable water content. In addition to limit the plastic strength of rocks (see equation (8)), fluids also play a critical role on their density such that:

$$\rho_{eff} \; = \; \rho_{rock} \left(1 - \; X_{fluid}\right) + \; \rho_{fluid}\, X_{fluid} \;, \tag{11}$$

with

$$\rho_{rock} \; = \; \rho_0 \left(1 - \; \alpha \, (T - 298)\right) \left(1 + \; \beta \, (P - 0.1)\right) . \tag{12}$$

Further details on the fluid implementation are available in Gerya & Meilick (2011) and Menant et al. (2019).

The top of the lithospheres is solved as an internal free surface by using a low-viscosity layer, which minimizes shear stresses at air-rock interface and leads to an accurate estimation of topographic variations associated with subduction-related deep processes (Schmeling et al., 2008; Crameri et al., 2012). Furthermore, sedimentation and erosion processes are also considered by applying the following equation at the surface (Gorczyk et al., 2007):

$$\frac{\partial y_{surf}}{\partial t} \; = \; v_y - v_x \frac{\partial y_{surf}}{\partial x} - v_{sedim} + \; v_{erosion} \;, \tag{13}$$

with (i) $v_{erosion}$ = 0.3 mm yr^{-1} and v_{sedim} = 0 mm yr^{-1} for y < 10 km (i.e., above the prescribed sea level) and (ii) $v_{erosion}$ = v_{sedim} = 0 mm yr^{-1} for y > 10 km (i.e., below the prescribed sea level). A modified erosion/sedimentation rate of 1 mm yr^{-1} is applied in regions with steep surface slopes (i.e., >17 °) in order to account for additional mass transport.

Supplementary Table 1. List of symbols used in the equations.

Symbols	Description
A_D	Pre-exponential factor
α	Thermal expansion
β	Compressibility
C	Cohesion
C_P	Isobaric heat capacity
E	Activation energy
$\dot{\varepsilon}_{ij}$	Deviatoric strain rate tensor
$\dot{\varepsilon}_{ij_{elastic}}$	Elastic component of the deviatoric strain rate tensor
$\dot{\varepsilon}_{ij_{plastic}}$	Plastic component of the deviatoric strain rate tensor
$\dot{\varepsilon}_{ij_{viscous}}$	Viscous component of the deviatoric strain rate tensor
$\dot{\varepsilon}_{II}$	Second invariant of the strain rate tensor
φ_{dry}	Internal friction angle for dry rock
g_i	Gravitational acceleration vector (g_x *= 0;* g_y *= 9.81 m s*$^{-2}$)
H_a	Adiabatic heat production
H_r	Radiogenic heat production
H_s	Shear heating
k	Thermal conductivity
λ_{fluid}	Pore fluid pressure factor (λ_{fluid}*= 0 for dry rocks;* λ_{fluid}*= 0.99 for fluid-oversaturated rocks*)
n	Creep exponent
η_{eff}	Effective creep viscosity
P	Pressure
q_i	Heat flux
R	Gas constant
ρ_{eff}	Effective rock density
ρ_{0solid}	Standard rock density
ρ_{crust}	Reference crust density (ρ_{crust} *= 2300 kg m*$^{-3}$)
ρ_{fluid}	Reference fluid density (ρ_{fluid} *= 1000 kg m*$^{-3}$)
σ_{ij}	Deviatoric stress tensor
σ_{yield}	Plastic strength
t	Time
T	Temperature
v_i	Viscous velocity vector
$v_{i_{water}}$	Fluid-marker velocity vector
v_{perc}	Reference percolation velocity
$v_{erosion}$	Erosion velocity
v_{sedim}	Sedimentation velocity
V	Activation volume
x_i	Spatial coordinates x and *y*
X_{fluid}	Mass fraction of fluid

Supplementary Table 2. Thermo-mechanical parameters used in numerical experiments. (*1*) Ranalli, 1995; (*2*) Hilairet et al., 2007.

	Ductile rheology					Plastic rheology		Elastic properties
Material	Flow law	Pre-exponential factor A_{D} (Pa^{-n} s^{-1})	Creep exponent n	Activation energy E (J mol^{-1})	Activation volume V (J Pa^{-1} mol^{-1})	Cohesion (Pa)	Internal friction angle $\sin(\varphi_{\mathrm{dry}})$	Shear modulus μ (Pa)
Sediments	Wet quartzite *(1)*	1.97×10^{17}	2.3	1.54×10^{5}	8.0×10^{-6}	1.0×10^{7}	0.15	1.0×10^{10}
Upper continental crust	Wet quartzite *(1)*	1.97×10^{17}	2.3	1.54×10^{5}	1.2×10^{-5}	1.0×10^{7}	0.15	2.5×10^{10}
Lower continental crust	Plagioclase An_{75} *(1)*	4.80×10^{22}	3.2	2.38×10^{5}	8.0×10^{-6}	1.0×10^{7}	0.15	2.5×10^{10}
Basaltic crust	Plagioclase An_{75} *(1)*	4.80×10^{22}	3.2	2.38×10^{5}	8.0×10^{-6}	1.0×10^{7}	0.65	2.5×10^{10}
Gabbroic crust	Diabase *(1)*	1.26×10^{24}	3.4	2.60×10^{5}	8.0×10^{-6}	1.0×10^{7}	0.60	2.5×10^{10}
Dry mantle	Dry olivine *(1)*	3.98×10^{16}	3.5	5.32×10^{5}	8.0×10^{-6}	1.0×10^{7}	0.60	6.7×10^{10}
Hydrated mantle	Wet olivine *(1)*	5.01×10^{20}	4.0	4.70×10^{5}	8.0×10^{-6}	1.0×10^{7}	0.10	6.7×10^{10}
Serpentinized mantle	Serpentine *(2)*	3.21×10^{36}	3.8	8.90×10^{3}	3.2×10^{-8}	1.0×10^{7}	0.10	6.7×10^{10}
Hydrated mantle (initial weak zone)	Wet olivine *(1)*	5.01×10^{20}	4.0	4.70×10^{5}	8.0×10^{-6}	1.0×10^{7}	0.10	6.7×10^{10}

Supplementary Table 2 *(continued)*.

	Density calculation			Heat conservation equation		
Material	Density ρ_0	Thermal expansion α	Compressibility β	Isobaric heat capacity C_p	Thermal conductivity k	Radiogenic heat production H_r
	(kg m^{-3})	(K^{-1})	(Pa^{-1})	(J kg^{-1} K^{-1})	(W m^{-1} K^{-1})	(W kg^{-1})
Sediments	2600	3.0×10^{-5}	1.0×10^{-11}	1.0×10^{3}	[0.64+807/(T+77)] exp (4*P*)	2.0×10^{-6}
Upper continental crust	2700	3.0×10^{-5}	1.0×10^{-11}	1.0×10^{3}	[0.64+807/(T+77)] exp (4*P*)	1.0×10^{-6}
Lower continental crust	2950	3.0×10^{-5}	1.0×10^{-11}	1.0×10^{3}	[1.18+474/(T+77)] exp (4*P*)	1.0×10^{-6}
Basaltic crust	3000	3.0×10^{-5}	1.0×10^{-11}	1.0×10^{3}	[1.18+474/(T+77)] exp (4*P*)	2.5×10^{-7}
Gabbroic crust	3000	3.0×10^{-5}	1.0×10^{-11}	1.0×10^{3}	[1.18+474/(T+77)] exp (4*P*)	2.5×10^{-7}
Dry mantle	3200	3.0×10^{-5}	1.0×10^{-11}	1.0×10^{3}	[0.73+1293/(T+77)] exp (4*P*)	2.2×10^{-8}
Hydrated mantle	3200	3.0×10^{-5}	1.0×10^{-11}	1.0×10^{3}	[0.73+1293/(T+77)] exp (4*P*)	2.2×10^{-8}
Serpentinized mantle	3000	3.0×10^{-5}	1.0×10^{-11}	1.0×10^{3}	[0.73+1293/(T+77)] exp (4*P*)	2.2×10^{-8}
Hydrated mantle (initial weak zone)	3200	3.0×10^{-5}	1.0×10^{-11}	1.0×10^{3}	[0.73+1293/(T+77)] exp (4*P*)	2.2×10^{-8}

Transient accretionary-erosive regime at forearc margins: new insights from alternative numerical experiments

Variations in deep accretion and erosion regimes along active margins have long been thought to depend on the amount of sediments entering the trench (Clift & Vannucchi, 2004) or on the subduction of oceanic plateaus, ridges, large seamount chains or oceanic fracture zones (e.g., Bourgois et al., 1996; Ranero & von Huene, 2000; Moreno et al., 2014; Vogt & Gerya, 2014). Indeed, as they are buried along with the oceanic crust, these large "asperities" may modify durably the rheological properties of the subducting interface, which have a first-order control on tectonic underplating (Agard et al. 2018; Menant et al., 2019). The comparison of the two main numerical experiments presented in this study (models *Steady-5* and *Transient-5*) supports this hypothesis and further show that the switch from an accretive to an erosive margin occurs through a 10s-Myr-long transitional period where frontal and shallow basal erosion processes are coeval with deep underplating (**Figs. 8-11**; see details in the main text). In the following section, we investigate the impact of varying the size of the subducting rheological asperity and of the plate-convergence rate on the development of this transient accretionary-erosive regime through a series of alternative experiments designed from model *Transient-5*. The aim of these additional simulations is obviously not to investigate the full range of subduction-related parameters that may modulate the margin dynamics but rather focus on the accurate comprehension of this critical transient subduction regime and associated geological records.

Margin dynamics and subduction of small asperities (model* Transient100-5*)

In this experiment, we prescribed the subduction of a 100-km-wide, dry and strong oceanic crust segment after 18 Myr (**Supplementary Fig. 1**; see also *Supplementary Movie 3*). The first-order model evolution leads to the formation of a wide frontal prism and a thick duplex at the base of the forearc crust, which supports a high coastal topography (**Supplementary Figs. 1a, b, d**). In terms of forearc deformation, the model predicts thrusting events at the toe of the margin and normal faulting at ~100 km landward from the trench, accommodating the exhumation and the doming of the duplex underneath (**Supplementary Fig. 1c**). This nearly steady-state accretionary regime is only disrupted by an episode of basal erosion at ~23-25 Myr following the subduction of a 100-km wide segment of strong oceanic crust (see *Supplementary Movie 3* for a better visualization). The lack of significant changes in the forearc deformation pattern prevent the tectonic record of this off-scraping event, which can only be suspected by the recognition of an age gap in the regularly-spaced sequence of deep accretionary events through detailed geochronological investigations on paleo-duplex structures (e.g., Grove et al., 2008; Angiboust et al., 2018). At the surface, this transient erosive phase is expressed by a ~2-Myr-long period of subsidence of the outer forearc domain, which may be hardly distinguishable from the uplift-then-subsidence sequences characterizing the succession of underplating events (**Supplementary Fig. 1d**; see also **Fig. 11a**).

To summarize, this additional experiment suggests that the subduction of small asperities does not modify significantly the margin dynamics. Instead, they cause only minor disruptions in the accretion/erosion regime, which may be difficult to track in the geological records.

Transient accretionary-erosive regime and plate-convergence rate (models* Transient-10 *and* Transient-2*)

Plate-convergence rate plays a critical role on the thermal structure, stress loading and mass flux in subduction zones. To evaluate the impact of this parameter, we set up two additional simulations with ~10- and ~2-cm yr^{-1} plate-convergence rate, respectively.

The fast-subduction experiment (model *Transient-10*; **Supplementary Fig. 2**; see also *Supplementary Movie 4*) predicts three different subduction regimes. (i) From 0 to ~11 Myr, a typical accretionary margin develops with frontal and basal accretion leading to the growth of a wide frontal wedge and a duplex (i.e., duplex #1; **Supplementary Fig. 2a**). (ii) At ~11 Myr, a transient accretionary-erosive stage starts in response to the subduction of the dry and strong oceanic crust (**Supplementary Fig. 2b**). The frontal wedge and duplex #1 are then rapidly consumed by frontal and basal erosion, while a second nappe stack is formed at higher depth (i.e., duplex #2) from tectonically eroded material (i.e., mostly sediments and basaltic crust). Forearc deformation characterizing this accretionary-erosive margin includes local thrusting accommodating differential basal-erosion rate along the plate interface and normal faulting above the deep duplex (**Supplementary Fig. 2c**). At the surface, landward trench retreat and subsidence characterise the outer forearc domain which experiences tectonic erosion, while a ~5-Myr-long uplift event is predicted landward in response to deep underplating, resulting in the rise of a high coastal topography (i.e., forearc high #2; **Supplementary Fig. 2d**). (iii) Finally, the duplex #2 is also dismembered after ~20 Myr as the basal-erosion front propagates downward, making the margin dynamics fully erosive with widespread forearc subsidence (*Supplementary Movie 4*). This evolution is similar to the main experiment *Transient-5* (**Figs. 9, 11**) but with a faster kinematics and thus a shorter transient accretionary-erosive stage (i.e., lasting ~10 Myr and ~22 Myr for models *Transient-10* and *Transient-5*, respectively).

The slow-subduction experiment (model *Transient-2*; **Supplementary Fig. 3**; see also *Supplementary Movie 5*) displays a different evolution. During the first accretionary stage (i.e., from 0 to ~42 Myr), frontal and basal accretion takes place through an overall horizontal flow contributing to the formation of a thick accretionary wedge (**Supplementary Fig. 3a**). As suggested by Menant et al. (2020), the dominant slicing of mafic crust is promoted by the low material influx (and the small amount of subducting sediments) associated with the slow plate-convergence rate. Resulting less-buoyant, basalt-rich wedge prevents its vertical exhumation (unlike the buoyant, sediment-rich duplex predicted in the faster simulations) and favours, instead, a plate-motion-driven horizontal flow and a low forearc topography (**Supplementary Fig. 3d**). After ~42 Myr, the subduction of the dry and strong oceanic crust triggers the propagation of the tectonic-erosion front downdip, which leads to modify the subduction regime from accretional to erosive in ~10 Myr (**Supplementary Fig. 3b**; see also *Supplementary Movie 5*). However, unlike the faster simulations, the dismembering of the former accretionary wedge is very slow, preventing a massive mass influx in the subduction channel and therefore the formation of a deeper, transient duplex. At the surface, the development of the erosive margin is first marked by a ~2 Myr-long uplift event marking the slightly increasing mass flux triggered by tectonic erosion and, then, by the landward retreat of the trench and the collapse of the outer forearc domain (**Supplementary Fig. 3d**). Forearc deformation is dominated by thrusting affecting the accretionary wedge during the entire model experiment (**Supplementary Fig. 3c**). In addition, minor extensional deformation is predicted in the shallowest part of the forearc domain, first onshore and then propagating offshore when the margin becomes erosive.

To conclude, these two additional experiments show that plate kinematics controls (i) the duration of the transient accretion-erosion event leading to the switch from typically accretionary to erosive margin (i.e., the faster the plate-convergence rate, the shorter the transient period) and (ii) the formation of transient deep duplexes by acting on the amount of material entering the subduction channel (i.e., buried from the trench or scrapped off by tectonic erosion). This points out the significance of the ratio between the mass flux and the capacity of the subduction channel to consume this inflow as it critically affects the distribution of accretion and tectonic erosion processes both in space (i.e., along the plate interface) and time (i.e., during the subduction of large asperities).

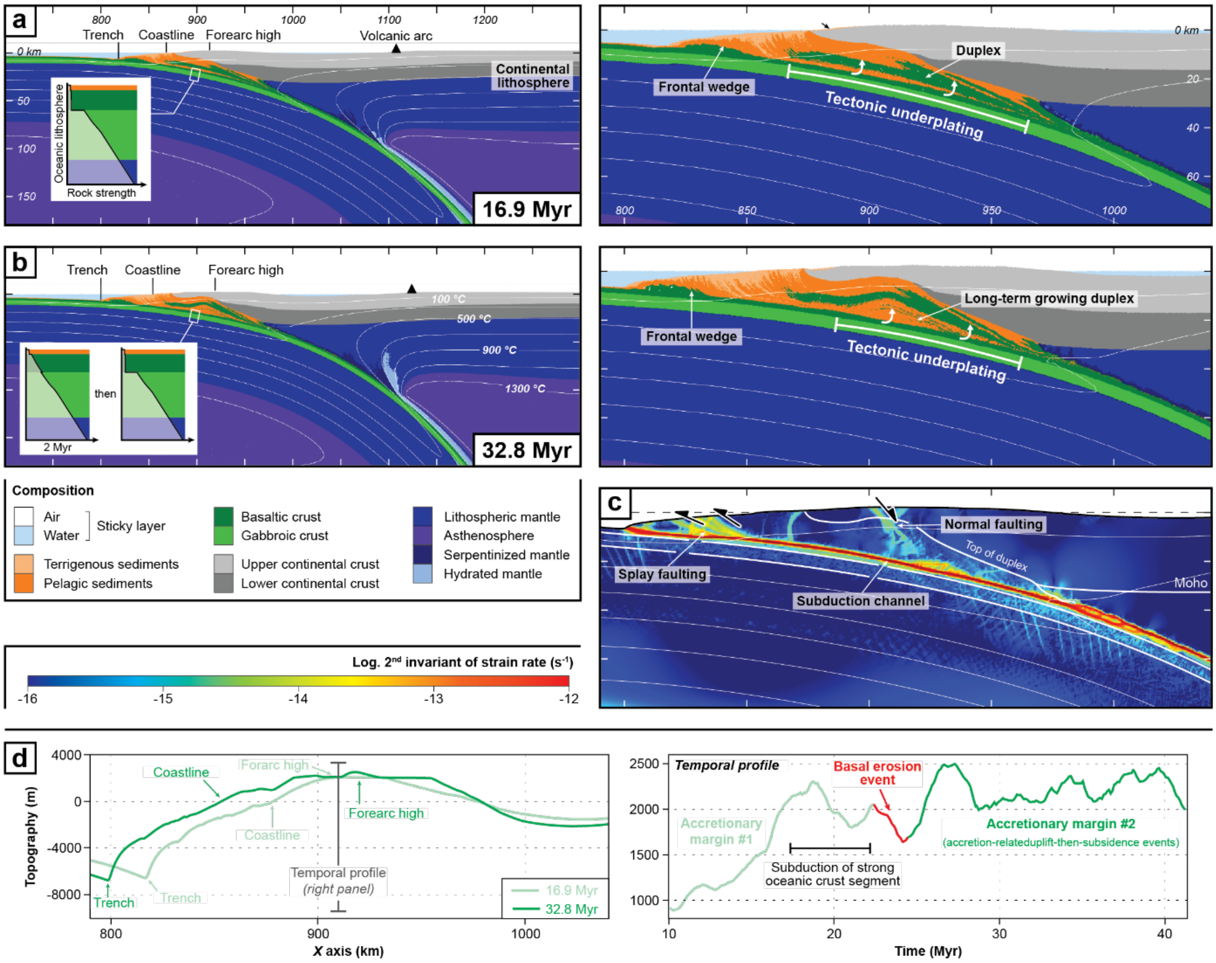

Supplementary Figure 1. Numerical results of model *Transient100-5* where a 100-km-long segment of dry and strong oceanic crust subducts at ~18 Myr. (a) Composition maps of the first accretionary stage (large-scale view and zoom on the forearc domain) predicting the formation of a frontal and basal accretionary wedge. (b) Composition maps of the second accretionary stage ~32 Myr after the subduction of the strong oceanic crust segment (large-scale view and zoom on the forearc domain). Insets on left panels (a) and (b) show the relative strength of the subducting lithosphere during the model evolution. (c) Strain-rate map showing the typical deformation pattern affecting the forearc domain during the second accretionary stage. (d) Forearc topographic profiles during the two accretionary stages (left panel) and temporal profile of vertical surface evolution of the forearc domain (right panel).

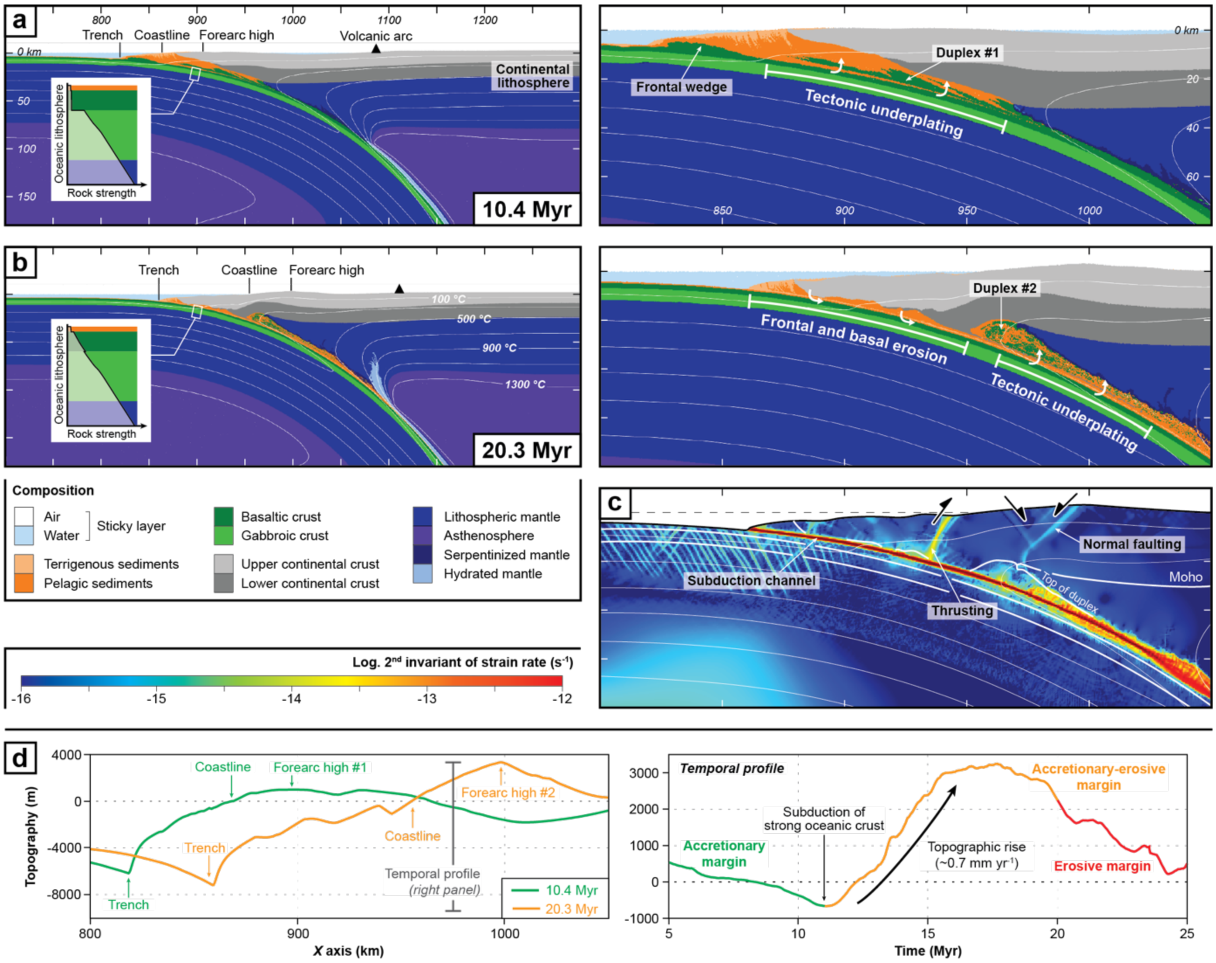

Supplementary Figure 2. Numerical results of fast-subduction model *Transient-10* (V_{conv} = ~10 cm yr^{-1}) where the rheological properties of the subducting oceanic crust have been modified after ~11 Myr to reproduce an accretionary-then-erosive margin. (a) Composition maps of the accretionary stage (large-scale view and zoom on the forearc domain) predicting the formation of a frontal and basal accretionary wedge. (b) Composition maps of the transient accretionary-erosive stage (large-scale view and zoom on the forearc domain) where frontal and shallow basal erosion are coeval with deep underplating, resulting in the formation of the deep duplex #2. Insets on left panels (a) and (b) show the relative strength of the subducting lithosphere during these two stages. (c) Strain-rate map showing the typical deformation pattern affecting the forearc domain during the accretionary-erosive stage. (d) Forearc topographic profiles of the accretionary and accretionary-erosive margins (left panel) and temporal profile of vertical surface evolution of the forearc domain from the accretionary to the erosive stage (right panel).

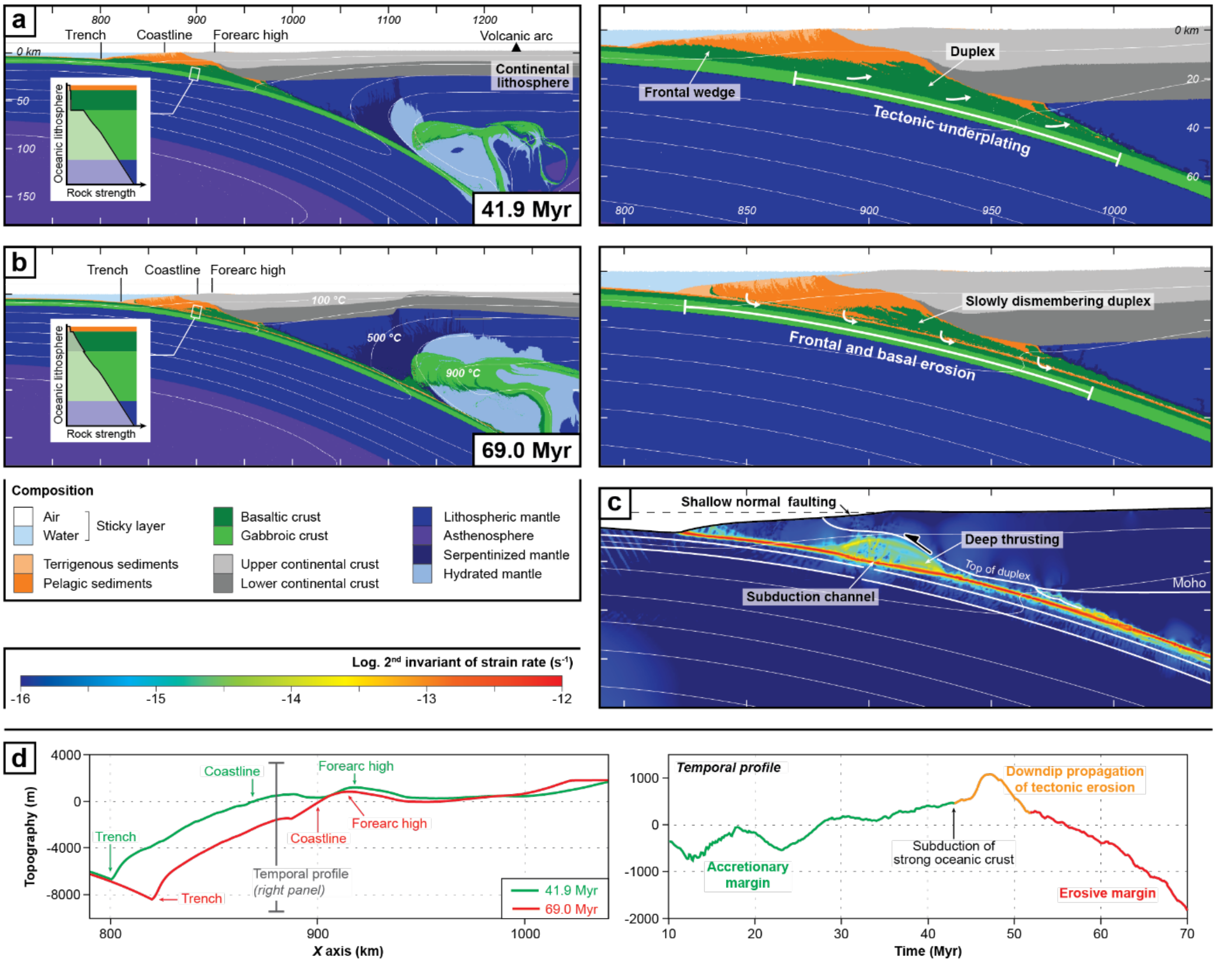

Supplementary Figure 3. Numerical results of slow-subduction model *Transient-2* (V_{conv} = ~2 cm yr^{-1}) where the rheological properties of the subducting oceanic crust have been modified after ~42 Myr to reproduce an accretionary-then-erosive margin. (a) Composition maps of the accretionary stage (large-scale view and zoom on the forearc domain) predicting the formation of a frontal and basal accretionary wedge. (b) Composition maps of the erosive stage (large-scale view and zoom on the forearc domain) where frontal and basal erosion slowly dismembers the former accretionary wedge. Insets on left panels (a) and (b) show the relative strength of the subducting lithosphere during these two stages. (c) Strain-rate map showing the typical deformation pattern affecting the forearc domain during the erosive stage. (d) Forearc topographic profiles of the accretionary and erosive margins (left panel) and temporal profile of vertical surface evolution of the forearc domain from the accretionary to the erosive stage (right panel).

References

Agard, P., Plunder, A., Angiboust, S., Bonnet, G., & Ruh, J. (2018). The subduction plate interface: rock record and mechanical coupling (from long to short timescales). *Lithos*, *320*, 537-566.

Angiboust, S., Cambeses, A., Hyppolito, T., Glodny, J., Monié, P., Calderón, M., & Juliani, C. (2018). A 100-my-long window onto mass-flow processes in the Patagonian Mesozoic subduction zone (Diego de Almagro Island, Chile). *Bulletin*, *130*(9-10), 1439-1456.

Bourgois, J., Martin, H., Lagabrielle, Y., Le Moigne, J., & Frutos Jara, J. (1996). Subduction erosion related to spreading-ridge subduction: Taitao peninsula (Chile margin triple junction area). *Geology*, *24*(8), 723-726.

Clift, P., & Vannucchi, P. (2004). Controls on tectonic accretion versus erosion in subduction zones: Implications for the origin and recycling of the continental crust. *Reviews of Geophysics*, *42*(2).

Connolly, J. A. (2005). Computation of phase equilibria by linear programming: a tool for geodynamic modeling and its application to subduction zone decarbonation. *Earth and Planetary Science Letters*, *236*(1-2), 524-541.

Crameri, F., Schmeling, H., Golabek, G. J., Duretz, T., Orendt, R., Buiter, S. J. H., ... & Tackley, P. J. (2012). A comparison of numerical surface topography calculations in geodynamic modelling: an evaluation of the 'sticky air'method. *Geophysical Journal International*, *189*(1), 38-54.

Gerya, T. V., & Yuen, D. A. (2003). Characteristics-based marker-in-cell method with conservative finite-differences schemes for modeling geological flows with strongly variable transport properties. *Physics of the Earth and Planetary Interiors*, *140*(4), 293-318.

Gerya, T. V., & Yuen, D. A. (2007). Robust characteristics method for modelling multiphase visco-elasto-plastic thermo-mechanical problems. *Physics of the Earth and Planetary Interiors*, *163*(1-4), 83-105.

Gerya, T. V., & Meilick, F. I. (2011). Geodynamic regimes of subduction under an active margin: effects of rheological weakening by fluids and melts. *Journal of Metamorphic Geology*, *29*(1), 7-31.

Gorczyk, W., Willner, A. P., Gerya, T. V., Connolly, J. A., & Burg, J. P. (2007). Physical controls of magmatic productivity at Pacific-type convergent margins: Numerical modelling. *Physics of the Earth and Planetary Interiors*, *163*(1-4), 209-232.

Grove, M., Bebout, G. E., Jacobson, C. E., Barth, A. P., Kimbrough, D. L., King, R. L., ... & Draut, A. E. (2008). The Catalina Schist: evidence for middle Cretaceous subduction erosion of southwestern North America. *SPECIAL PAPERS-GEOLOGICAL SOCIETY OF AMERICA*, *436*, 335.

Hilairet, N., Reynard, B., Wang, Y., Daniel, I., Merkel, S., Nishiyama, N., & Petitgirard, S. (2007). High-pressure creep of serpentine, interseismic deformation, and initiation of subduction. *Science*, *318*(5858), 1910-1913.

Menant, A., Angiboust, S., & Gerya, T. (2019). Stress-driven fluid flow controls long-term megathrust strength and deep accretionary dynamics. *Scientific reports*, *9*(1), 1-11.

Menant, A., Angiboust, S., Gerya, T., Lacassin, R., Simoes, M., & Grandin, R. (2020). Transient stripping of subducting slabs controls periodic forearc uplift. *Nature communications*, *11*(1), 1-10.

Moore, J. C., & Vrolijk, P. (1992). Fluids in accretionary prisms. *Reviews of Geophysics*, *30*(2), 113-135.

Moreno, M., Haberland, C., Oncken, O., Rietbrock, A., Angiboust, S., & Heidbach, O. (2014). Locking of the Chile subduction zone controlled by fluid pressure before the 2010 earthquake. *Nature Geoscience*, *7*(4), 292-296.

Peacock, S. A. (1990). Fluid processes in subduction zones. *Science*, *248*(4953), 329-337.

Ranalli, G. (1995). *Rheology of the Earth*. Springer Science & Business Media.

Ranero, C. R., & von Huene, R. (2000). Subduction erosion along the Middle America convergent margin. *Nature*, *404*(6779), 748-752.

Saffer, D. M., & Tobin, H. J. (2011). Hydrogeology and mechanics of subduction zone forearcs: Fluid flow and pore pressure. *Annual Review of Earth and Planetary Sciences*, *39*, 157-186.

Schmeling, H., Babeyko, A. Y., Enns, A., Faccenna, C., Funiciello, F., Gerya, T., ... & Schmalholz, S. M. (2008). A benchmark comparison of spontaneous subduction models—Towards a free surface. *Physics of the Earth and Planetary Interiors*, *171*(1-4), 198-223.

Vogt, K., & Gerya, T. V. (2014). From oceanic plateaus to allochthonous terranes: numerical modelling. *Gondwana Research*, *25*(2), 494-508.